Superposition of nonparaxial vectorial complex-source spherically focused beams: Axial Poynting singularity and reverse propagation

F. G. Mitri
Chevron, Area 52 Technology–ETC, 5 Bisbee Court, Santa Fe, New Mexico 87508, USA
(Received 27 April 2016; published 1 August 2016)

In this work, counterintuitive effects such as the generation of an axial (i.e., long the direction of wave motion) zero-energy flux density (i.e., axial Poynting singularity) and reverse (i.e., negative) propagation of nonparaxial quasi-Gaussian electromagnetic (EM) beams are examined. Generalized analytical expressions for the EM field's components of a coherent superposition of two high-order quasi-Gaussian vortex beams of opposite handedness and different amplitudes are derived based on the complex-source-point method, stemming from Maxwell's vector equations and the Lorenz gauge condition. The general solutions exhibiting unusual effects satisfy the Helmholtz and Maxwell's equations. The EM beam components are characterized by nonzero integer degree and order (n,m), respectively, an arbitrary waist w_0, a diffraction convergence length known as the Rayleigh range z_R, and a weighting (real) factor $0 \leqslant \alpha \leqslant 1$ that describes the transition of the beam from a purely vortex ($\alpha = 0$) to a nonvortex ($\alpha = 1$) type. An attractive feature for this superposition is the description of strongly focused (or strongly divergent) wave fields. Computations of the EM power density as well as the linear and angular momentum density fluxes illustrate the analysis with particular emphasis on the polarization states of the vector potentials forming the beams and the weight of the coherent beam superposition causing the transition from the vortex to the nonvortex type. Should some conditions determined by the polarization state of the vector potentials and the beam parameters be met, an axial zero-energy flux density is predicted in addition to a negative retrograde propagation effect. Moreover, rotation reversal of the angular momentum flux density with respect to the beam handedness is anticipated, suggesting the possible generation of negative (left-handed) torques. The results are particularly useful in applications involving the design of strongly focused optical laser tweezers, tractor beams, optical spanners, arbitrary scattering, radiation force, angular momentum, and torque in particle manipulation, and other related topics.

DOI: 10.1103/PhysRevA.94.023801

I. INTRODUCTION

Scalar waves with a Gaussian beam profile originate in the wave diffraction theory as a solution of the parabolic (paraxial) wave equation (pp. 143–156 in Ref. [1], pp. 637–641 in Ref. [2], and pp. 263–287 in Ref. [3]). Various mathematical models were developed for beam-forming design purposes to describe the propagation of weakly focused or quasicollimated beams [4–7], as well as evaluating the beam-shape coefficients (BSCs) [8,9], which are essential in computing the scattering, radiation force, and torque on particles placed arbitrarily in the field of electromagnetic (EM) or optical beams [8,10]. For tightly focused beams, improved models [11–13] have been developed based on the angular spectrum decomposition approach [14], finite series (Chap. V in Ref. [8]), and the formalism of localized beams (Chap. VII in Ref. [8]), which produce a remodeled Maxwellian beam that closely resembles the original paraxial beam. Other models based on the complex rays [15–18] and the complex-source-point methods [19–29] have been devised, which produce exact solutions of Maxwell's equations, without the need of the higher-order corrections [6,7,9,30] required to regularize the paraxial Gaussian beam and make its mathematical expression suitable for computational purposes.

One particular solution has been developed [27], which is a fundamental (zeroth-order) beam description of a generalized result [28] corresponding to a higher-order quasi-Gaussian vortex beam satisfying Maxwell's equations. The generalized solution has been termed high-order "quasi-Gaussian" to make a distinction from the paraxial Gaussian beam that does not satisfy Maxwell's equations. The mathematical expressions for the EM field's components of a generalized high-order quasi-Gaussian *vortex* beam in a complex coordinates system consist of products of spherical Bessel functions of the first kind and associated Legendre functions with a complex exponential phase dependency on the azimuthal angle.

In this work, the complex-source-point is further extended to develop the most general solution corresponding to a transition from a vortex to a nonvortex high-order quasi-Gaussian beam of any integer degree and order (n,m) which satisfies the Helmholtz and Maxwell's equations. It is shown here that it is possible to create a coherent superposition of two copropagating high-order quasi-Gaussian vortex beams of opposite handedness (i.e., opposite helicity or topological charge) and different amplitude. Depending on the amplitude difference between the two beams, the resulting field can carry a total angular momentum (i.e., beam of vortex nature), or not (i.e., beam of nonvortex type). Stemming from the Lorenz gauge condition [31], Maxwell's equations, and the state of polarization of the vector potentials, closed-form expressions for the EM field's components are established without any approximations. Moreover, the EM power density and the linear and angular momentum flux densities are examined. Numerical computations illustrate the analysis with particular emphasis on the polarization state of the vector potential from which the EM fields are derived and the weight of the coherent superposition. The results anticipate the production of an axial (i.e., along the direction of wave motion) Poynting singularity (i.e., axial zero-energy density flux). In general, the Poynting vector is a real observable; thus, it has no phase

associated with it, and subsequently, it does not possess any *phase* singularities. On the other hand, the Poynting "singularity" encountered here results from the indeterminacy of its direction at zero amplitude. Since the Poynting vector is a composite observable resulting from the interaction of the electric and magnetic fields, the singularity can arise due to the vector field singularities (i.e., zeros of the electric and magnetic field) and the mutual polarization of the fields. Moreover, negative-energy flux density in the axial direction is observed in a bounded region around the axis where the local behavior of the wave field is similar to that of a wave field with negative-energy flow. This physical phenomenon observed using strongly focused quasi-Gaussian beams is of essential importance for EM and optical traps and tweezers, where the location as well as the linear and angular momenta may be manipulated by varying the sign of the Poynting vector. The zero- and negative-energy flux density characteristics of the quasi-Gaussian (vortex) solution may also be used in invisibility cloaks, such that a metamaterial object could possibly tailor the incident wavefront into a quasi-Gaussian field propagating in the host medium. Furthermore, a sign reversal of the forward linear and angular momentum flux densities is predicted, which may suggest the possible generation of retrograde wave propagation and negative (left-handed) torques [32,33] should some conditions related to the beam parameters be adequately satisfied. The physical properties and characteristics of the generalized quasi-Gaussian (vortex) beam solution developed here are necessary to study for design optimization purposes of a possible improved generation of laser beams with strong focusing. Notice that the mathematical modeling of strongly focused optical (vortex) beams remains among the hot topics of modern optics due to its utility in the prediction of counterintuitive effects from the standpoint of EM wave propagation theory and polarization. The present solution and associated results should also be of potential interest to investigations involving the study of the arbitrary scattering by strongly focused optical beams, radiation force, and torque, as well as the quantitative predictions of the linear and angular momenta of tightly focused (or strongly divergent), and quasicollimated high-order quasi-Gaussian beams.

II. METHOD

The propagation of a monochromatic beam with a harmonic time dependence of $\exp(-i\omega t)$ in vacuum is assumed. The time-harmonic dependence is dropped from all subsequent terms for convenience. Consider a magnetic vector potential field $\mathbf{A}_{H,x}$ describing a superposition of two propagating high-order quasi-Gaussian vortex beams with opposite handedness and different amplitudes, and expressed in complex coordinates as

$$\begin{aligned}\mathbf{A}_{H,x} &= A\mathbf{x}, \\ &= \frac{A_0}{2} e^{-kz_R} j_n(\kappa_\pm) P_n^m(\cos\theta_\pm)[e^{im\phi} + \alpha e^{-im\phi}]\mathbf{x}, \end{aligned} \quad (1)$$

where $\mathbf{x}$ is the unit vector along the x direction; A_0 is the characteristic amplitude; $\kappa_\pm = kR_\pm$, where k is the wave number of the incident radiation; $j_n(\cdot)$ is the spherical Bessel function of the first kind that is nonsingular at the origin $R_\pm = 0$; $P_n^m(\cdot)$ are the associated Legendre functions of integer degree n and order m; $R_\pm = \sqrt{x^2 + y^2 + Z_\pm^2}$, $\theta_\pm = \cos^{-1}(Z_\pm/R_\pm)$, $\phi = \tan^{-1}(y/x)$, where the inverse tangent must be suitably defined taking into account the correct quadrant of (x,y); $Z_\pm = (z \pm iz_R)$; e^{-kz_R} is a normalization constant; $z_R = (kw_0^2)/2$ is known as the Rayleigh range; w_0 is the beam waist; and α is a real number representing the amplitude ratio of the superposition of the two beams (i.e., the weighted sum). When $\alpha = 0$, the beam is of vortex nature (i.e., the azimuthal dependence is expressed under the form of a complex exponential function), whereas when $\alpha = 1$, the beam becomes of trigonometric (nonvortex) type (i.e., the azimuthal dependence is expressed under the form of a cosine function [34,35]). In this sense, the parameter α describes the transition from vortex to nonvortex behavior of the high-order quasi-Gaussian beam. Moreover, since each individual component is an exact solution of the Helmholtz equation [21], their superposition as given by Eq. (1) also satisfies the Helmholtz wave equation.

Using the Lorenz gauge condition [31], a magnetic field $\mathbf{H}_H$ is defined as

$$\nabla \times \mathbf{A}_{H,x} = \mathbf{H}_H. \quad (2)$$

Thus, from Maxwell's equations and Eq. (2), the electric field is expressed as

$$\mathbf{E}_H = ik[\mathbf{A}_{H,x} + \nabla(\nabla \cdot \mathbf{A}_{H,x})/k^2]. \quad (3)$$

The Cartesian components of the EM field can now be determined from these equations. However, the generalized description of beams in free space (with no specific boundary conditions imposed) requires adding the dual field setup to Eqs. (1)–(3) in the process of deriving the EM beam components, which represent symmetry in their mathematical expressions. In other words, if only Eqs. (1)–(3) were used, the resulting electric and magnetic fields would be nonsymmetric. However, to describe a circularly symmetric quasi-Gaussian beam in free space, both the electric and magnetic fields must exhibit symmetry. Therefore, the procedure requires defining a second electric vector potential field $\mathbf{A}_{E,y}$ polarized along the negative (or positive) y direction such that

$$\mathbf{A}_{E,y} = -A\mathbf{y}, \quad (4)$$

where $\mathbf{y}$ is the unit vector along the y direction. Therefore, an electric field $\mathbf{E}_E$ may be defined as

$$\nabla \times \mathbf{A}_{E,y} = \mathbf{E}_E. \quad (5)$$

Thus, from Maxwell's equations and Eq. (5), the magnetic field is expressed as

$$\mathbf{H}_E = -ik[\mathbf{A}_{E,y} + \nabla(\nabla \cdot \mathbf{A}_{E,y})/k^2]. \quad (6)$$

Adding the solution of Eqs. (2) and (3) to the solution of Eqs. (5) and (6), and dividing the end result by 2 leads to the spatial Cartesian components for the superposition of high-order quasi-Gaussian vortex beams such that the electric and magnetic vector fields are expressed, respectively, as $\mathbf{E}^u = \frac{1}{2}(\mathbf{E}_E + \mathbf{E}_H)$ and $\mathbf{H}^u = \frac{1}{2}(\mathbf{H}_E + \mathbf{H}_H)$, where $\mathbf{E}^u = (E_x^u, E_y^u, E_z^u)$ and $\mathbf{H}^u = (H_x^u, H_y^u, H_z^u)$. The superscript u denotes the state of polarization of the vector potentials, such that $u = (x, -y)$ defines the fields obtained based on the

polarizations chosen in Eqs. (1) and (4). The results for the fields are given in Eqs. (A2)–(A7) in the Appendix.

It has already been established that the polarization of the vector potentials can have significant impact on the mathematical expressions and spatial distributions of the EM field's components [27,28]. Changing the transverse polarization to an axial (i.e., along the direction z) one requires choosing another set of vector potentials, for example, the first, $\mathbf{A}_{H,z}$, polarized along the direction of wave propagation, z, and the second vector potential $\mathbf{A}_{E,z}$, polarized along the opposite direction, $-z$. Note that this type of (axial) polarization has been previously suggested for the development of a new type of free-electron laser [36]. Repeating the derivations for this choice of potentials [defined as the $u = (z,-z)$ configuration], produces a set of spatial Cartesian components given by Eqs. (A8)–(A13) in the Appendix that differ from Eqs. (A3)–(A7) for the $u = (x,-y)$ polarization configuration.

After derivation of the EM field's components, other observables, such as the time-averaged Poynting vector $\langle \mathbf{S} \rangle$ as well as the linear and angular momentum density fluxes can be evaluated. The EM power density (i.e., time-averaged Poynting vector) is expressed as (p. 259 in Ref. [31])

$$\begin{aligned}\langle \mathbf{S}^u \rangle &= \frac{c}{8\pi}\mathrm{Re}\{\mathbf{E}^u \times \mathbf{H}^{u*}\} \\ &= \frac{c}{8\pi}\mathrm{Re}\left\{S_x^u\mathbf{x} + S_y^u\mathbf{y} + S_z^u\mathbf{z}\right\} \\ &= \frac{c}{8\pi}\mathrm{Re}\begin{Bmatrix}\left(E_y^u H_z^{u*} - E_z^u H_y^{u*}\right)\mathbf{x} \\ +\left(E_z^u H_x^{u*} - E_x^u H_z^{u*}\right)\mathbf{y} \\ +\left(E_x^u H_y^{u*} - E_y^u H_x^{u*}\right)\mathbf{z}\end{Bmatrix},\end{aligned} \tag{7}$$

where $\mathbf{z}$ is the unit vector along the z direction, the symbol $\langle\cdot\rangle$ denotes time averaging, Re[·] denotes the real part of a complex number, and the superscript * indicates a complex conjugate.

In the following, the analysis is extended to include the description of the axial components of the time-averaged linear and angular momenta density fluxes.

The expression for the *linear momentum* flux density tensor in vacuum is given by (p. 261 in Ref. [31]), $\overleftrightarrow{\mathbf{\Pi}}^u = (W^u \overleftrightarrow{\mathbf{I}} - \mathbf{E}^u \otimes \mathbf{E}^u - \mathbf{H}^u \otimes \mathbf{H}^u)$, where the energy density for the free EM field is $W^u = \frac{1}{2}[E^{u^2} + H^{u^2}]$; $\overleftrightarrow{\mathbf{I}}$ is the identity matrix (tensor); $\otimes$ denotes a tensor product, with $\overleftrightarrow{\mathbf{\Pi}}^u = -\overleftrightarrow{\mathrm{T}}^u$, where $\overleftrightarrow{\mathrm{T}}^u$ is known as the Minkowski form of Maxwell's stress tensor [31,37,38]. It follows that the axial component of the time-averaged linear momentum density flux (which can cause an *axial* force [10] if a particle is placed along the waves path) is expressed as

$$\begin{aligned}\Pi_{zz}^u &= \mathbf{z}^T \langle \overleftrightarrow{\mathbf{\Pi}}^u \rangle \mathbf{z}, \\ &= \tfrac{1}{4}\left[\left|E_x^u\right|^2 + \left|E_y^u\right|^2 - \left|E_z^u\right|^2 + \left|H_x^u\right|^2 + \left|H_y^u\right|^2 - \left|H_z^u\right|^2\right],\end{aligned} \tag{8}$$

where the superscript T denotes the transpose of a vector.

Moreover, the angular momentum density flux tensor is $\overleftrightarrow{\mathbf{M}}^u = \mathbf{r} \times \overleftrightarrow{\mathbf{\Pi}}^u$. This angular momentum can produce a torque on a particle [10], which can be determined by performing a surface integration of the dot product of the outwardly directed normal unit vector and the negative angular momentum density flux tensor.

The angular momentum flux density tensor is expressed as

$$\overleftrightarrow{\mathbf{M}}^u = W^u \mathbf{r} \times \overleftrightarrow{\mathbf{I}} - (\mathbf{r} \times \mathbf{E}^u) \otimes \mathbf{E}^u - (\mathbf{r} \times \mathbf{H}^u) \otimes \mathbf{H}^u. \tag{9}$$

For time-harmonic wave fields, $\langle \overleftrightarrow{\mathbf{M}}^u \rangle$ is solenoidal; i.e., $\nabla \cdot \langle \overleftrightarrow{\mathbf{M}}^u \rangle = 0$. Moreover, it is noticed that the energy density factor W^u does not contribute to the diagonal components of $\overleftrightarrow{\mathbf{M}}^u$ in Eq. (9), but only the off-diagonal terms. It follows that the axial component of the time-averaged angular momentum density flux tensor is expressed as [39]

$$\begin{aligned}M_{zz}^u &= \mathbf{z}^T \langle \overleftrightarrow{\mathbf{M}}^u \rangle \mathbf{z}, \\ &= \tfrac{1}{2}\mathrm{Re}\left[y\left(E_x^u E_z^{u*} + H_x^u H_z^{u*}\right) - x\left(E_y^u E_z^{u*} + H_y^u H_z^{u*}\right)\right].\end{aligned} \tag{10}$$

III. NUMERICAL RESULTS AND DISCUSSIONS

To illustrate the analysis from the standpoint of energy characteristics as well as the linear and angular momentum density fluxes of the superposition of nonparaxial EM first-order quasi-Gaussian (denoted by SqG_{11}) focused vortex beams, numerical computations are performed by considering a nondimensional beam waist $kw_0 = 3$ (corresponding to a tightly focused beam). However, in the simulations $n = m = 1$, the analytical development is applicable to any integer values (nm). Notice that in optical systems the diffraction limit is usually reached for a beam waist w_0 approaching half the wavelength $\lambda/2$ of the incident radiation (i.e., $kw_0 = \pi$) [2]. A superposition of qG_{nm} beams with $kw_0 < 3$ results in a beam that is not directional and may not be entirely physically realizable [40]. Below this limit, wave reflections at the aperture of the focused source would practically generate exponentially decaying evanescent waves which become relatively important as $kw_0 \to 0$. Nonetheless, because of its exponential distance dependence, evanescent waves would yield infinite energy at a distance far away from the origin. Thus, on physical grounds, evanescent waves cannot exist in free-space and their generation is restricted to the aperture of the optical source.

All the components for the Poynting vector, in addition to the axial (i.e., along z) components of the linear and angular momentum density fluxes given by Eqs. (7), (8), and (10), respectively, are numerically evaluated in the nondimensional transverse plane $-10 \leqslant (kx,ky) \leqslant 10$ for a SqG_{11} (i.e., $n = m = 1$) propagating in free-space with particular emphasis on the superposition parameter α and type of polarization of the vector potentials.

Figures 1(a)–1(c) show the plots for the axial energy flux density $S_{z,11}$ for the transverse $(x,-y)$ polarization case, and for $\alpha = 0$. The axial energy density flux is maximal around the center of the "hollow" beam as shown in Fig. 1(c). Moreover, Fig. 1(d) explicitly shows that the axial energy flux density is *negative* around the central axis region, suggesting reverse beam propagation. Notice that an analogous effect has been previously observed for vector Bessel (nondifracting) beams derived based on the superposition of TE- and TM-polarized

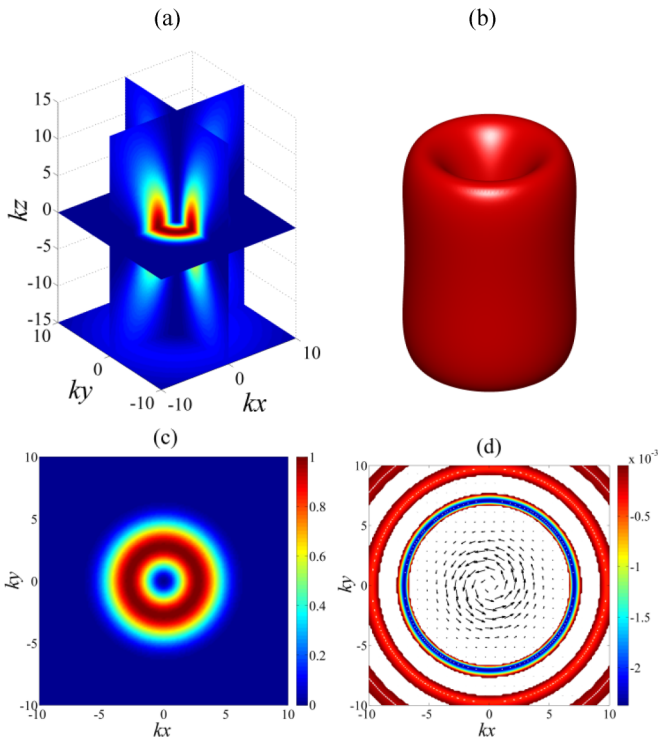

FIG. 1. (a)–(c) display the plots for the *axial* energy density flux for a SqG_{11} beam with $kw_0 = 3$ and $\alpha = 0$ with transverse $u = (x,-y)$ polarization. (b) represents the three-dimensional isosurface plot while (c) shows the cross-sectional transverse plot at $kz = 0$. (d) shows the plot for $S_{z,11} \leqslant 0$ where the transverse Poynting vector field $\mathbf{S}^{u}_{\perp,11} = (S^{u}_{x,11}, S^{u}_{y,11})$ computations (denoted by the vector arrows) are superimposed on the plots of the axial component $S_{z,11} \leqslant 0$.

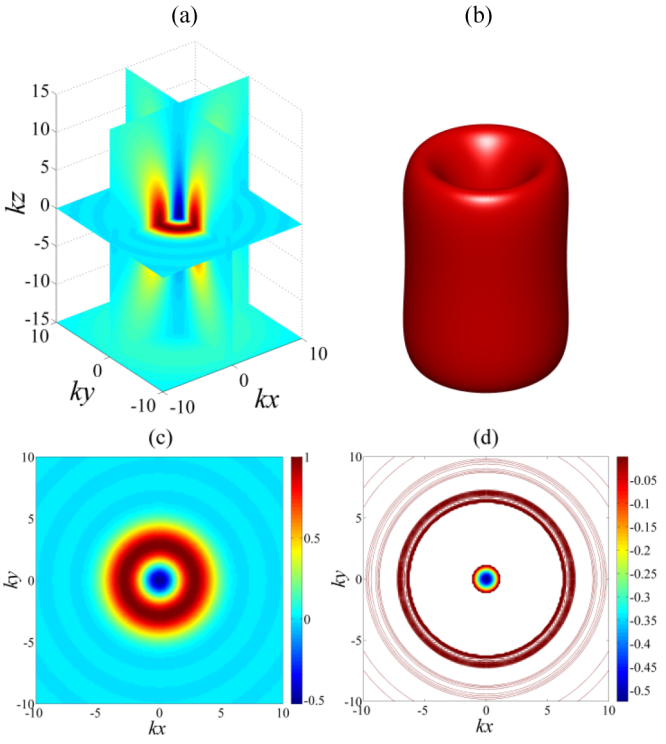

FIG. 2. The plots for the axial linear momentum density flux $\Pi^{(x,-y)}_{zz,11}$ for a SqG_{11} beam with $kw_0 = 3$ and $\alpha = 0$ with transverse $u = (x,-y)$ polarization. (d) shows the values over which $\Pi^{(x,-y)}_{zz,11} \leqslant 0$.

beams [41], and x-wave [42] and Airy beams [43] which differ from the generalized SqG_{nm} solution presented here. Figure 1(d) shows the plot for $S_{z,11} \leqslant 0$ where the transverse Poynting vector field $\mathbf{S}^{(x,-y)}_{\perp,11} = (S^{(x,-y)}_{x,11}, S^{(x,-y)}_{y,11})$ computations (denoted by the vector arrows) are superimposed on the plots of the axial component $S^{(x,-y)}_{z,11} \leqslant 0$. The anticlockwise direction of rotation of the vector arrows of $\mathbf{S}^{(x,-y)}_{\perp,11}$ shows the vortex nature of the transverse vector energy density flux. In addition, the negative regions of the axial energy density flux in Fig. 1(d) are delimited by circular lines over which $S^{(x,-y)}_{z,11} = 0$. This corresponds to an "axial" Poynting singularity [44] where the axial energy density flux of the incident beam vanishes.

Figures 2(a)–2(d) display the computational plots for the axial component of the linear momentum density flux tensor. Figure 2(d) shows that negative values for $\Pi^{(x,-y)}_{zz,11}$ are indeed possible, which are maximal at the center of the beam. This effect suggests that it may be possible to induce a retrograde motion on a particle placed around or at the central region of the beam, depending on its intrinsic physical properties. Moreover, $\Pi^{(x,-y)}_{zz,11}$ vanishes along lines delimiting annular regions over which $\Pi^{(x,-y)}_{zz,11} < 0$.

Similar to the axial Poynting singularity mentioned earlier, the effect of having conditions where $\Pi^{(x,-y)}_{zz,11} = 0$ such that the incident field does not induce any linear momentum density flux in the axial direction corresponds to a linear momentum density flux singularity.

Figures 3(a)–3(d) display the computational plots for the axial angular momentum density flux. Depending on the amount of the shift from the center of the beam, $M^{(x,-y)}_{zz,11}$ vanishes before it becomes negative over annular regions delimited by angular momentum singularity lines (where $M^{(x,-y)}_{zz,11} = 0$) as explicitly shown in Fig. 3(d). The negative amplitude is maximal over the first annular region around the central axis, and vanishes at the center of the beam. The sign reversal suggests that the axial angular momentum flux density (which is responsible for creating an orbital torque on a particle located arbitrarily in space) has an opposite handedness with respect to the beam's transverse Poynting vector $\mathbf{S}^{(x,-y)}_{\perp,11}$ shown in Fig. 1(d). This could lead to the generation of a *negative* radiation torque that can rotate a particle in a reversed angular direction to that of $\mathbf{S}^{(x,-y)}_{\perp,11}$.

The effect of changing the polarization of the incident SqG_{11} vortex beam is investigated such that an axial $(z,-z)$ state is now considered. The corresponding results are displayed in Figs. 4–6 for the Poyting vector components, and axial linear and angular momentum flux densities, respectively. In contrast with the results obtained for the transverse $(x,-y)$ polarization shown in Figs. 1–3, the axial component $S^{(z,-z)}_{z,11}$ is *maximal* at the center of the beam as shown in Figs. 4(a)–4(c), though the beam remains of vortex nature as shown in Fig. 4(d) (i.e., vector arrows with anticlockwise direction of rotation). Moreover, $\Pi^{(z,-z)}_{zz,11}$ displays a different behavior than the one observed for $\Pi^{(x,-y)}_{zz,11}$ by comparison of Fig. 5 with Fig. 2.

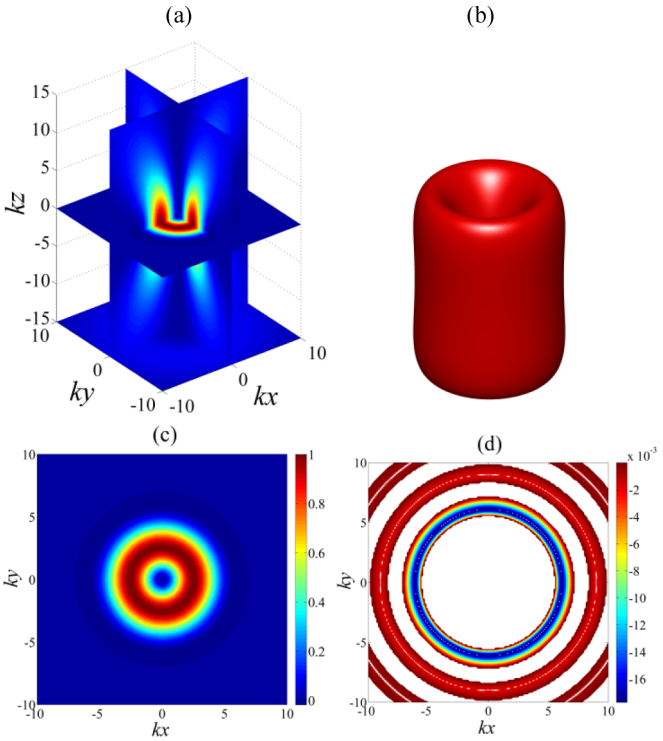

FIG. 3. The plots for the axial angular momentum density flux $M^{(x,-y)}_{zz,11}$ for a SqG_{11} beam with $kw_0 = 3$ and $\alpha = 0$ with transverse u=$(x,-y)$ polarization. (d) shows the values over which $M^{(x,-y)}_{zz,11} \leqslant 0$.

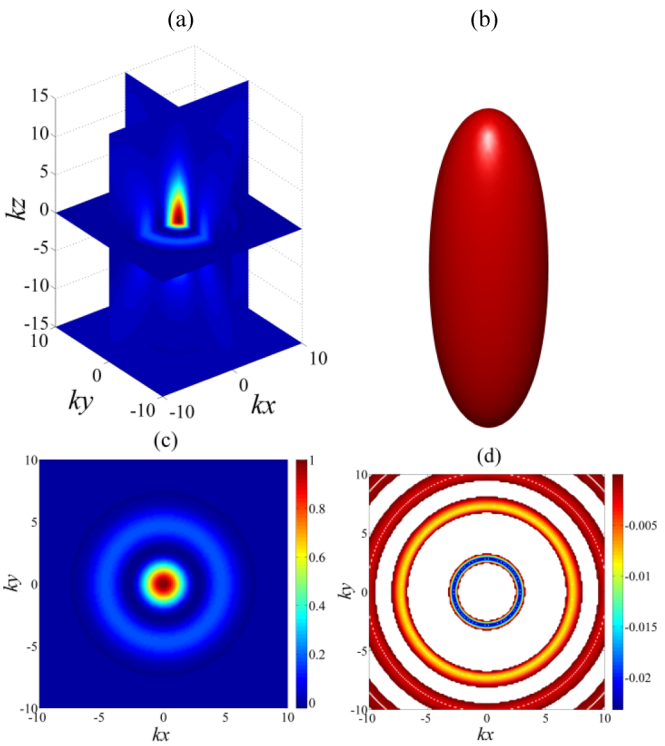

FIG. 5. The same as in Fig. 2 but an axial polarization $(z,-z)$ for the vector potentials is considered.

At the center of the beam in Fig. 5, $\Pi^{(z,-z)}_{zz,11} > 0$, while it vanishes before becoming negative over an annular region around the central axis. Furthermore, Fig. 5(d) shows that the negative amplitudes are smaller than those obtained for $\Pi^{(x,-y)}_{zz,11}$ as shown in Fig. 2(d). As for $M^{(z,-z)}_{zz,11}$, Fig. 6 shows that a comparable behavior to $M^{(x,-y)}_{zz,11}$ in Fig. 3 is observed;

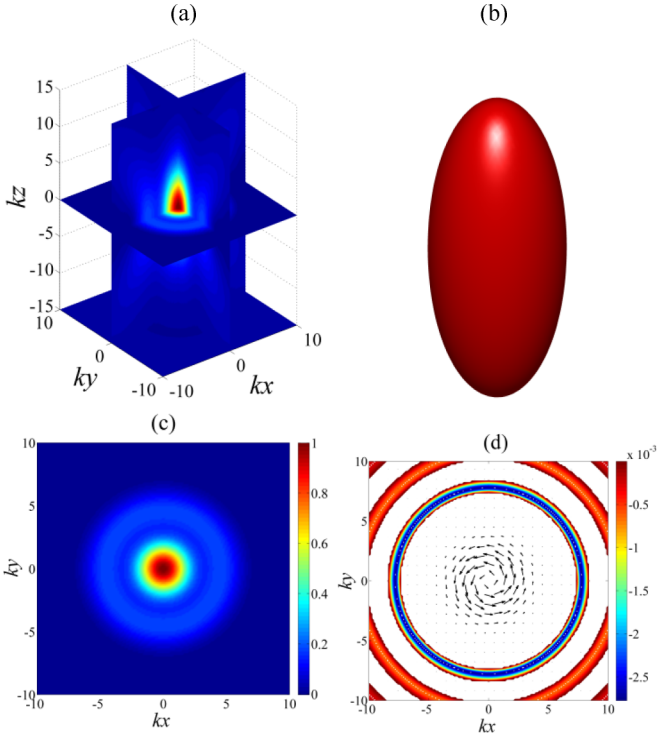

FIG. 4. The same as in Fig. 1 but an axial polarization $(z,-z)$ for the vector potentials is considered.

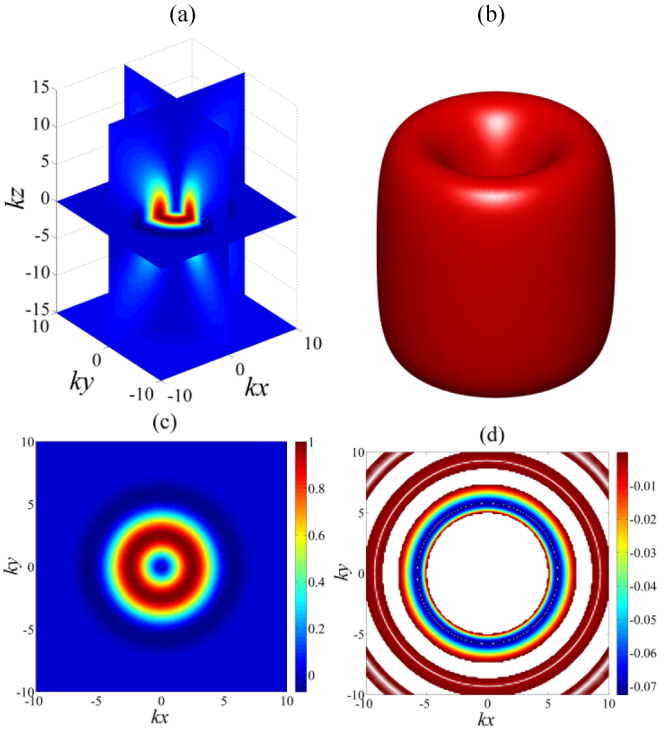

FIG. 6. The same as in Fig. 3 but an axial polarization $(z,-z)$ for the vector potentials is considered.

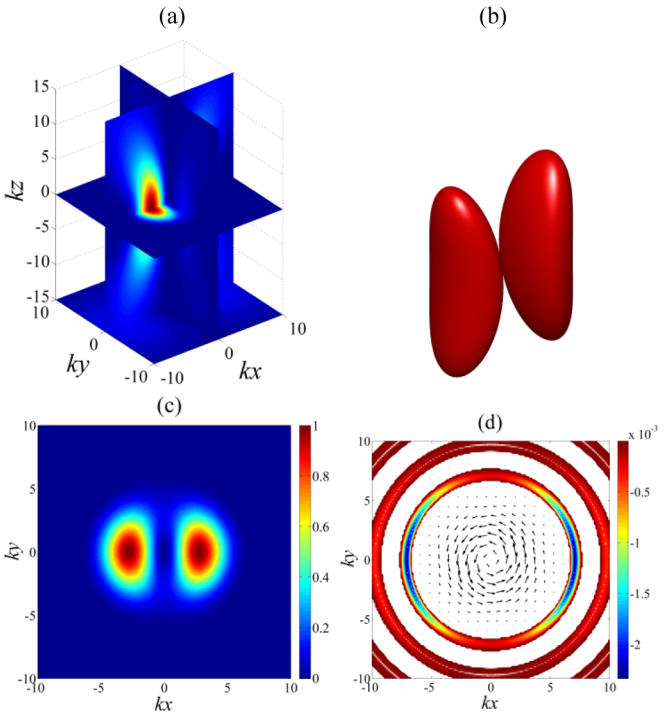

FIG. 7. The same as in Fig. 1 but $\alpha = 0.5$.

$M_{zz,11}^{(z,-z)}$ is maximal over an annular region around the axis before it vanishes and becomes negative. Notice, however, that the negative amplitudes are larger than those obtained for $M_{zz,11}^{(x,-y)}$ as shown by comparing Figs. 3(d) and 6(d).

The weight of the superposition of nonparaxial vectorial complex-source spherically focused beam solutions is now investigated, such that $\alpha = 0.5$. The corresponding plots for this configuration are shown in Figs. 7(a)–7(d), 8(a)–8(d), and 9(a)–9(d) for the Poyting vector components, and axial linear and angular momentum flux densities, respectively. The transverse polarization $(x,-y)$ case is only considered since the axial $(z,-z)$ state displays similar effects. A one-to-one

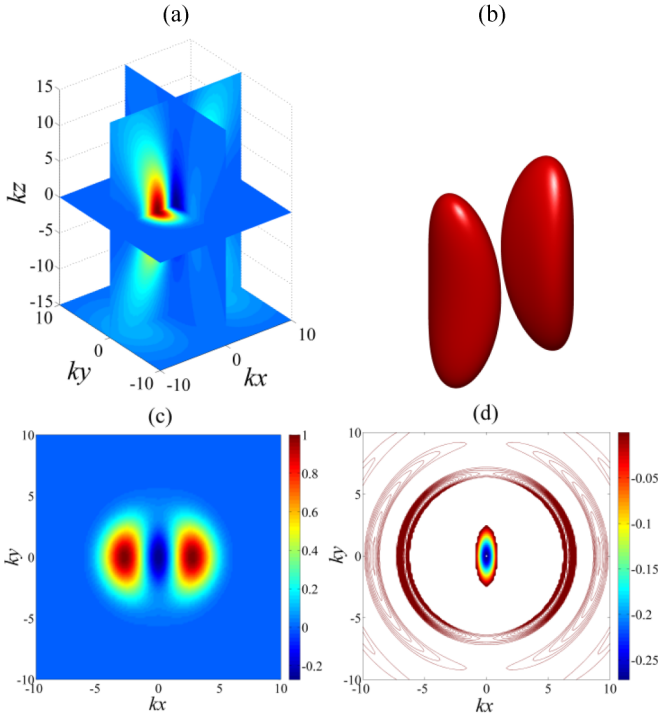

FIG. 8. The same as in Fig. 2 but $\alpha = 0.5$.

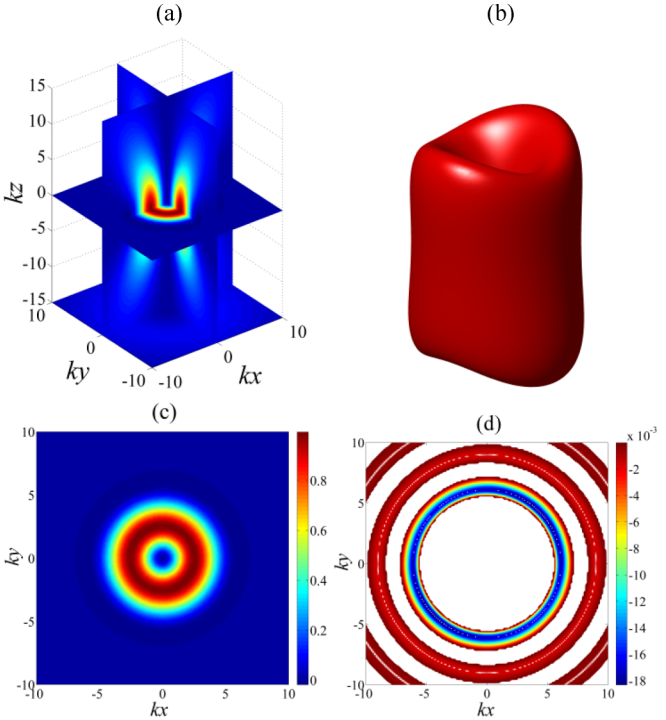

FIG. 9. The same as in Fig. 3 but $\alpha = 0.5$.

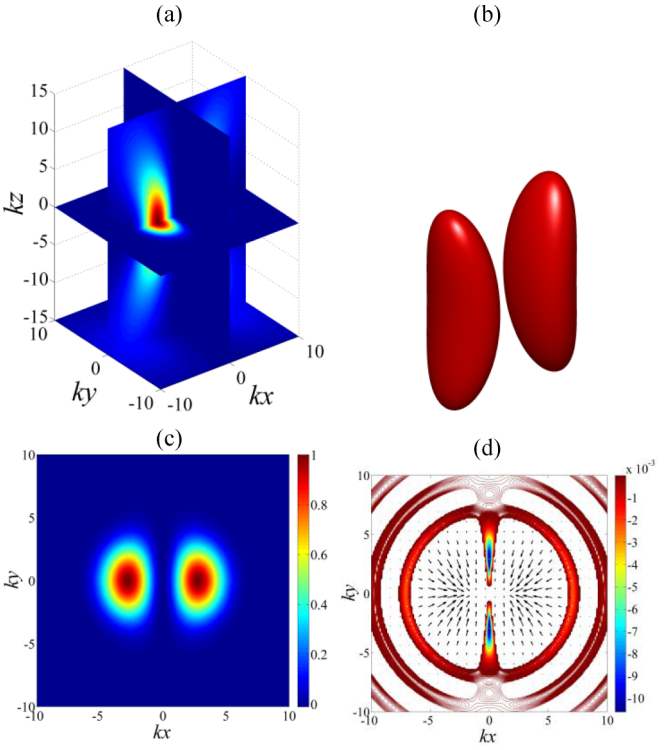

FIG. 10. The same as in Fig. 1 but $\alpha = 1$.

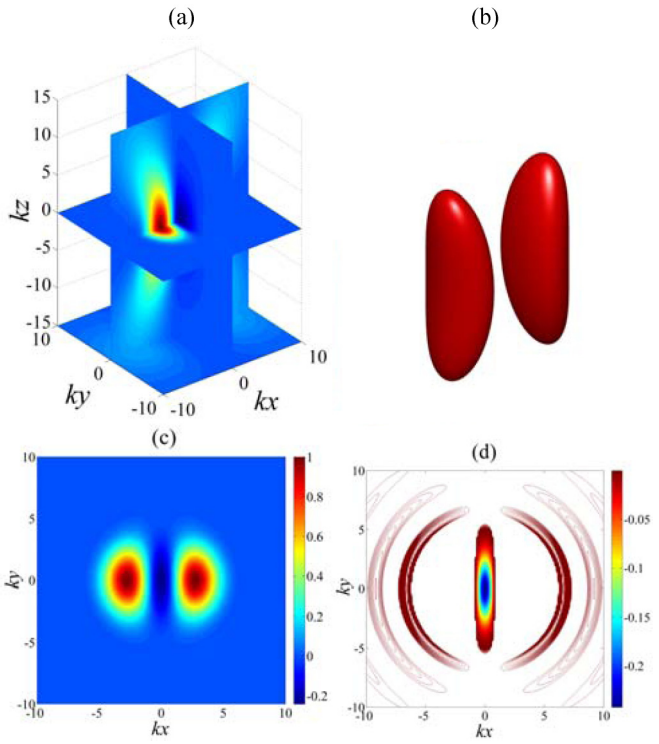

FIG. 11. The same as in Fig. 2 but $\alpha = 1$.

comparison of the figures with those of Figs. 1–3 shows that the superposition affects the spatial distribution of the physical observables in the (kx,ky) plane. For Figs. 7 and 8, respectively, the circular symmetry (observed previously for Figs. 1 and 2) is broken. Nonetheless, the vortex nature of the transverse Poynting vector is still manifested as shown in Fig. 7(d). Notice also that the plots for $M_{zz,11}^{(x,-y)}$ of Fig. 9 preserve the circular symmetry. Moreover, all observables display singularities and negative values depending on the amount of the shift from the center of the beam.

The effect of further increasing the weighted sum parameter α to unity is shown in Figs. 10(a)–10(d) and 11(a)–11(d) for the Poyting vector components as well as the axial linear momentum flux density, respectively, in the transverse polarization $(x,-y)$ state. As shown in Fig. 10(d), the transverse Poynting vector displays a nonvortex behavior, with the Poynting vector arrows converging towards the central region. Nonetheless, an axial Poynting singularity is still manifested in the cross-sectional plane as well as negative values indicating reverse propagation. Moreover, Figs. 11(a)–11(d) show that the circular symmetry previously noted in Fig. 2 is broken for the axial linear momentum flux density while the central region over which $\Pi_{zz,11}^{(x,-y)} < 0$ is enlarged. Notice that for the nonvortex case (i.e., $\alpha = 1$), the axial angular momentum vanishes at the center of the beam.

IV. CONCLUSION

In summary, counterintuitive effects related to the coherent superposition of nonparaxial vectorial complex-source spherically focused beams are revealed from the standpoint of energy, linear, and angular momentum flux density characteristics. Zero-energy density flux as well as negative propagation in which the direction of the Poynting vector reverses sign during propagation have been theoretically studied. Should some conditions determined by the polarization type u, the weighted sum parameter α, and beam focusing properties be met, the axial components of the energy, linear, and angular momentum flux densities vanish before they reverse their sign. Such properties suggest retrograde translation and rotation reversal with respect to the beam handedness. It follows directly from the results which are especially relevant to particle manipulation and handling applications that a particulate matter in strongly focused quasi-Gaussian beams would interact with the EM field and experiences the effects of the negative-energy and linear and angular momentum flux densities. It is important to emphasize here that the angular momentum flux density can be separated into spin and orbital contributions [39], which may be transferred to the object being manipulated. Subsequently, negative orbital and spin torques [32,33] can arise depending on the object's physical properties. These peculiar properties might be of potential use in particle manipulation applications using laser EM or optical tweezers, tractor beams, and optical spanners, where micro- and nanoparticles are currently utilized. The quasi-Gaussian beam description of waves with tight focusing offers an improved exact solution due to the highly localized nature of the wave field, its strong gradient, and the flexibility in manipulating the propagation and energy flow characteristics. The negative-energy flux density characteristics of the quasi-Gaussian beam solution could possibly be used also in invisibility cloaks.

APPENDIX: FIELD EXPRESSIONS

Defining the following parameters as

$$\Psi_n = \{\kappa_\pm[j_{n-1}(\kappa_\pm) - j_{n+1}(\kappa_\pm)] - j_n(\kappa_\pm)\},$$

$$\xi_n = \{\kappa_\pm^2[j_{n-2}(\kappa_\pm) - 2j_n(\kappa_\pm) + j_{n+2}(\kappa_\pm)] + 2\kappa_\pm[j_{n+1}(\kappa_\pm) - j_{n-1}(\kappa_\pm)] + 3j_n(\kappa_\pm)\},$$

$$F_{nm} = \left[(n+1)Z_\pm P_n^m(\cos\theta_\pm) + (m-n-1)R_\pm P_{n+1}^m(\cos\theta_\pm)\right],$$

$$\chi_{nm} = \left[(m-n-1)Z_\pm P_{n+1}^m(\cos\theta_\pm) + \sqrt{R_\pm^2 - Z_\pm^2}\,P_{n+1}^{m+1}(\cos\theta_\pm)\right],$$

$$\Phi_{nm} = \left[(m-n-1)Z_\pm(m^2 - 2mn + m - 3n^2 - k^2Z_\pm^2 - n + 1)P_{n+1}^m(\cos\theta_\pm)\right.$$
$$\left. + (m^2 - n^2 - k^2Z_\pm^2)\sqrt{R_\pm^2 - Z_\pm^2}\,P_{n+1}^{m+1}(\cos\theta_\pm)\right],$$

$$\Gamma_{nm} = \left[(-2m^2 + m + 2n^2 + 3n + 1)Z_\pm P_{n+1}^m(\cos\theta_\pm) + \sqrt{R_\pm^2 - Z_\pm^2}\,P_{n+1}^{m+1}(\cos\theta_\pm)\right],$$
$$\Lambda_{nm} = \big(n(n+1)P_n^m(\cos\theta_\pm)Z_\pm^2 + (m-n-1)(2n+3)R_\pm Z_\pm P_{n+1}^m(\cos\theta_\pm) + R_\pm^2\big\{(n+1)P_n^m(\cos\theta_\pm) + [m^2 - (2n+3)m + n^2 + 3n + 2]P_{n+2}^m(\cos\theta_\pm)\big\}\big), \tag{A1}$$

the EM field's components in complex coordinates are now expressed as

$$E_{x,nm}^{(x,-y)} = \frac{A_0}{8}e^{-(im\phi+kz_R)}\Bigg\{\frac{4(\alpha+e^{2im\phi})j_n(\kappa_\pm)F_{nm}}{R_\pm^2} + \frac{2(\alpha+e^{2im\phi})Z_\pm P_n^m(\cos\theta_\pm)\Psi_n}{R_\pm^2} + ik\Bigg[4(\alpha+e^{2im\phi})j_n(\kappa_\pm)P_n^m(\cos\theta_\pm) + \frac{1}{k^2}\Bigg(\frac{4(\alpha+e^{2im\phi})j_n(\kappa_\pm)Z_\pm^2x^2[2Z_\pm F_{nm}+\Lambda_{nm}]}{R_\pm^4(Z_\pm^2-R_\pm^2)^2} + \frac{4(\alpha+e^{2im\phi})j_n(\kappa_\pm)Z_\pm F_{nm}}{R_\pm^2(Z_\pm^2-R_\pm^2)} + \frac{8i(e^{2im\phi}-\alpha)xym\,j_n(\kappa_\pm)Z_\pm F_{nm}}{R_\pm^2(R_\pm^2-Z_\pm^2)(x^2+y^2)} + \frac{4(\alpha+e^{2im\phi})x^2Z_\pm F_{nm}[3j_n(\kappa_\pm)-\Psi_n]}{R_\pm^4(R_\pm^2-Z_\pm^2)} - \frac{4my[e^{2im\phi}(my-2ix)+\alpha(my+2ix)]j_n(\kappa_\pm)P_n^m(\cos\theta_\pm)}{(x^2+y^2)^2} + \frac{2(\alpha+e^{2im\phi})P_n^m(\cos\theta_\pm)\Psi_n}{R_\pm^2} - \frac{4i(e^{2im\phi}-\alpha)mxyP_n^m(\cos\theta_\pm)\Psi_n}{R_\pm^2(x^2+y^2)} + \frac{2(\alpha+e^{2im\phi})x^2P_n^m(\cos\theta_\pm)}{R_\pm^4}\left[\frac{\xi_n}{2}-\Psi_n\right]\Bigg)\Bigg]\Bigg\}, \tag{A2}$$

$$E_{y,nm}^{(x,-y)} = \frac{iA_0}{8k}e^{-(im\phi+kz_R)}\Bigg\{\frac{4(\alpha+e^{2im\phi})j_n(\kappa_\pm)Z_\pm^2xy[2Z_\pm F_{nm}+\Lambda_{nm}]}{R_\pm^4(Z_\pm^2-R_\pm^2)^2} + \frac{4i(e^{2im\phi}-\alpha)m\,j_n(\kappa_\pm)Z_\pm F_{nm}[y^2-x^2]}{R_\pm^2(R_\pm^2-Z_\pm^2)(x^2+y^2)} + \frac{4(\alpha+e^{2im\phi})xyZ_\pm F_{nm}[\Psi_n-3j_n(\kappa_\pm)]}{R_\pm^4(Z_\pm^2-R_\pm^2)} + \frac{4im[\alpha(x^2-y^2-imxy)+e^{2im\phi}(y^2-x^2-imxy)]j_n(\kappa_\pm)P_n^m(\cos\theta_\pm)}{(x^2+y^2)^2} + \frac{2i(e^{2im\phi}-\alpha)mP_n^m(\cos\theta_\pm)\Psi_n[x^2-y^2]}{R_\pm^2(x^2+y^2)} + \frac{(\alpha+e^{2im\phi})xyP_n^m(\cos\theta_\pm)[\xi_n-2\Psi_n]}{R_\pm^4}\Bigg\}, \tag{A3}$$

$$E_{z,nm}^{(x,-y)} = \frac{A_0}{8}e^{-(im\phi+kz_R)}\Bigg\{\frac{4i(e^{2im\phi}-\alpha)ym\,j_n(\kappa_\pm)P_n^m(\cos\theta_\pm)}{(x^2+y^2)} - \frac{4(\alpha+e^{2im\phi})xZ_\pm j_n(\kappa_\pm)F_{nm}}{R_\pm^2(Z_\pm^2-R_\pm^2)} - \frac{2(\alpha+e^{2im\phi})xP_n^m(\cos\theta_\pm)\Psi_n}{R_\pm^2} + \frac{i}{k}\Bigg[\frac{2(\alpha+e^{2im\phi})Z_\pm x\{2j_n(\kappa_\pm)[Z_\pm F_{nm}-\Lambda_{nm}]-Z_\pm F_{nm}\Psi_n\}}{R_\pm^4(R_\pm^2-Z_\pm^2)} - \frac{2i(e^{2im\phi}-\alpha)myP_n^m(\cos\theta_\pm)Z_\pm\Psi_n}{R_\pm^2(x^2+y^2)} + \frac{(\alpha+e^{2im\phi})xP_n^m(\cos\theta_\pm)Z_\pm[\xi_n-2\Psi_n]}{R_\pm^4} + \frac{4(\alpha+e^{2im\phi})xj_n(\kappa_\pm)F_{nm}}{R_\pm^2(Z_\pm^2-R_\pm^2)} - \frac{4i(e^{2im\phi}-\alpha)ym\,j_n(\kappa_\pm)F_{nm}}{R_\pm^2(x^2+y^2)} + \frac{2(\alpha+e^{2im\phi})xF_{nm}\Psi_n}{R_\pm^4}\Bigg]\Bigg\}, \tag{A4}$$

$$H_{x,nm}^{(x,-y)} = E_{y,nm}^{(x,-y)}, \tag{A5}$$

$$H_{y,nm}^{(x,-y)} = \frac{A_0}{8}e^{-(im\phi+kz_R)}\Bigg\{\frac{4(\alpha+e^{2im\phi})j_n(\kappa_\pm)F_{nm}}{R_\pm^2} + \frac{2(\alpha+e^{2im\phi})Z_\pm P_n^m(\cos\theta_\pm)\Psi_n}{R_\pm^2} + ik\Bigg[4(\alpha+e^{2im\phi})j_n(\kappa_\pm)P_n^m(\cos\theta_\pm) + \frac{1}{k^2}\Bigg(\frac{4(\alpha+e^{2im\phi})j_n(\kappa_\pm)Z_\pm^2y^2[2Z_\pm F_{nm}+\Lambda_{nm}]}{R_\pm^4(Z_\pm^2-R_\pm^2)^2} + \frac{4(\alpha+e^{2im\phi})j_n(\kappa_\pm)Z_\pm F_{nm}}{R_\pm^2(Z_\pm^2-R_\pm^2)} - \frac{8i(e^{2im\phi}-\alpha)xym\,j_n(\kappa_\pm)Z_\pm F_{nm}}{R_\pm^2(R_\pm^2-Z_\pm^2)(x^2+y^2)} + \frac{4(\alpha+e^{2im\phi})y^2Z_\pm F_{nm}[3j_n(\kappa_\pm)-\Psi_n]}{R_\pm^4(R_\pm^2-Z_\pm^2)} - \frac{4mx[\alpha(mx-2iy)+e^{2im\phi}(mx+2iy)]j_n(\kappa_\pm)P_n^m(\cos\theta_\pm)}{(x^2+y^2)^2} + \frac{2(\alpha+e^{2im\phi})P_n^m(\cos\theta_\pm)\Psi_n}{R_\pm^2} + \frac{4i(e^{2im\phi}-\alpha)mxyP_n^m(\cos\theta_\pm)\Psi_n}{R_\pm^2(x^2+y^2)} + \frac{2(\alpha+e^{2im\phi})y^2P_n^m(\cos\theta_\pm)}{R_\pm^4}\left[\frac{\xi_n}{2}-\Psi_n\right]\Bigg)\Bigg]\Bigg\}, \tag{A6}$$

$$H_{z,nm}^{(x,-y)} = \frac{A_0}{8} e^{-(im\phi+kz_R)} \Bigg\{ -\frac{4i(e^{2im\phi}-\alpha)xm\, j_n(\kappa_\pm) P_n^m(\cos\theta_\pm)}{(x^2+y^2)} - \frac{4(\alpha+e^{2im\phi})yZ_\pm j_n(\kappa_\pm)F_{nm}}{R_\pm^2(Z_\pm^2-R_\pm^2)} - \frac{2(\alpha+e^{2im\phi})y P_n^m(\cos\theta_\pm)\Psi_n}{R_\pm^2}$$
$$+ \frac{i}{k}\Bigg[\frac{2(\alpha+e^{2im\phi})Z_\pm y\{2j_n(\kappa_\pm)[Z_\pm F_{nm}-\Lambda_{nm}]-Z_\pm F_{nm}\}\Psi_n}{R_\pm^4(R_\pm^2-Z_\pm^2)} + \frac{2i(e^{2im\phi}-\alpha)mx P_n^m(\cos\theta_\pm)Z_\pm\Psi_n}{R_\pm^2(x^2+y^2)}$$
$$+ \frac{(\alpha+e^{2im\phi})y P_n^m(\cos\theta_\pm)Z_\pm[\xi_n-2\Psi_n]}{R_\pm^4} + \frac{4(\alpha+e^{2im\phi})j_n(\kappa_\pm)yF_{nm}}{R_\pm^2(Z_\pm^2-R_\pm^2)} + \frac{4i(e^{2im\phi}-\alpha)xm\, j_n(\kappa_\pm)F_{nm}}{R_\pm^2(x^2+y^2)}$$
$$+ \frac{2(\alpha+e^{2im\phi})yF_{nm}\Psi_n}{R_\pm^4}\Bigg]\Bigg\}. \tag{A7}$$

In the axial polarization scheme denoted by $(z,-z)$, those components are given as

$$E_{x,nm}^{(z,-z)} = \frac{A_0}{8} e^{-(im\phi+kz_R)} \Bigg\{ -\frac{4i(e^{2im\phi}-\alpha)xm\, j_n(\kappa_\pm) P_n^m(\cos\theta_\pm)}{(x^2+y^2)} - \frac{4(\alpha+e^{2im\phi})yZ_\pm j_n(\kappa_\pm)F_{nm}}{R_\pm^2(Z_\pm^2-R_\pm^2)} - \frac{2(\alpha+e^{2im\phi})y P_n^m(\cos\theta_\pm)\Psi_n}{R_\pm^2}$$
$$+ \frac{i}{k}\Bigg[\frac{2(\alpha+e^{2im\phi})Z_\pm x\{2j_n(\kappa_\pm)[2Z_\pm F_{nm}+\Lambda_{nm}]+Z_\pm F_{nm}\Psi_n\}}{R_\pm^4(Z_\pm^2-R_\pm^2)} - \frac{2i(e^{2im\phi}-\alpha)my\big[P_n^m(\cos\theta_\pm)Z_\pm\Psi_n+2j_n(\kappa_\pm)F_{nm}\big]}{R_\pm^2(x^2+y^2)}$$
$$+ \frac{2(\alpha+e^{2im\phi})xF_{nm}\Psi_n}{R_\pm^4} + \frac{(\alpha+e^{2im\phi})x P_n^m(\cos\theta_\pm)Z_\pm[\xi_n-2\Psi_n]}{R_\pm^4} + \frac{4(\alpha+e^{2im\phi})x(3Z_\pm^2-R_\pm^2)j_n(\kappa_\pm)F_{nm}}{R_\pm^4(R_\pm^2-Z_\pm^2)}\Bigg]\Bigg\}, \tag{A8}$$

$$E_{y,nm}^{(z,-z)} = \frac{A_0}{8} e^{-(im\phi+kz_R)} \Bigg\{ -\frac{4i(e^{2im\phi}-\alpha)ym\, j_n(\kappa_\pm) P_n^m(\cos\theta_\pm)}{(x^2+y^2)} + \frac{4(\alpha+e^{2im\phi})xZ_\pm j_n(\kappa_\pm)F_{nm}}{R_\pm^2(Z_\pm^2-R_\pm^2)} + \frac{2(\alpha+e^{2im\phi})x P_n^m(\cos\theta_\pm)\Psi_n}{R_\pm^2}$$
$$+ \frac{i}{k}\Bigg[\frac{2(\alpha+e^{2im\phi})Z_\pm y\{2j_n(\kappa_\pm)[2Z_\pm F_{nm}+\Lambda_{nm}]+Z_\pm F_{nm}\Psi_n\}}{R_\pm^4(Z_\pm^2-R_\pm^2)} + \frac{2i(e^{2im\phi}-\alpha)mx\big[P_n^m(\cos\theta_\pm)Z_\pm\Psi_n+2j_n(\kappa_\pm)F_{nm}\big]}{R_\pm^2(x^2+y^2)}$$
$$+ \frac{2(\alpha+e^{2im\phi})yF_{nm}\Psi_n}{R_\pm^4} + \frac{y(\alpha+e^{2im\phi})P_n^m(\cos\theta_\pm)Z_\pm[\xi_n-2\Psi_n]}{R_\pm^4} + \frac{4(\alpha+e^{2im\phi})y(3Z_\pm^2-R_\pm^2)j_n(\kappa_\pm)F_{nm}}{R_\pm^4(R_\pm^2-Z_\pm^2)}\Bigg]\Bigg\}, \tag{A9}$$

$$E_{z,nm}^{(z,-z)} = \frac{e^{-(im\phi+kz_R)}A_0(\alpha+e^{2im\phi})}{2i\kappa_\pm R_\pm^4(m+n+1)}\{j_n(\kappa_\pm)[\kappa_\pm^2R_\pm^2\chi_{nm}+(4n^2-1)Z_\pm^2\chi_{nm}+R_\pm^2\Phi_{nm}]$$
$$-\kappa_\pm\, j_{n+1}(\kappa_\pm)[R_\pm^2\Gamma_{nm}+(2n-1)Z_\pm^2\chi_{nm}]\}, \tag{A10}$$

$$H_{x,nm}^{(z,-z)} = \frac{A_0}{8} e^{-(im\phi+kz_R)} \Bigg\{ \frac{4i(e^{2im\phi}-\alpha)xm\, j_n(\kappa_\pm) P_n^m(\cos\theta_\pm)}{(x^2+y^2)} + \frac{4(\alpha+e^{2im\phi})yZ_\pm j_n(\kappa_\pm)F_{nm}}{R_\pm^2(Z_\pm^2-R_\pm^2)} + \frac{2(\alpha+e^{2im\phi})y P_n^m(\cos\theta_\pm)\Psi_n}{R_\pm^2}$$
$$- \frac{i}{k}\Bigg[\frac{2(\alpha+e^{2im\phi})Z_\pm x\{2j_n(\kappa_\pm)[2Z_\pm F_{nm}+\Lambda_{nm}]+Z_\pm F_{nm}\Psi_n\}}{R_\pm^4(R_\pm^2-Z_\pm^2)}$$
$$+ \frac{2i(e^{2i|m|\phi}-\alpha)my\big[P_n^m(\cos\theta_\pm)Z_\pm\Psi_n+2j_n(\kappa_\pm)F_{nm}\big]}{R_\pm^2(x^2+y^2)} - \frac{2(\alpha+e^{2i|m|\phi})xF_{nm}\Psi_n}{R_\pm^4}$$
$$- \frac{(\alpha+e^{2im\phi})x P_n^{|m|}(\cos\theta_\pm)Z_\pm[\xi_n-2\Psi_n]}{R_\pm^4} - \frac{4(\alpha+e^{2im\phi})x(3Z_\pm^2-R_\pm^2)j_n(\kappa_\pm)F_{nm}}{R_\pm^4(R_\pm^2-Z_\pm^2)}\Bigg]\Bigg\}, \tag{A11}$$

$$H_{y,nm}^{(z,-z)} = \frac{A_0}{8} e^{-(im\phi+kz_R)} \Bigg\{ \frac{4i(e^{2im\phi}-\alpha)ym\, j_n(\kappa_\pm) P_n^m(\cos\theta_\pm)}{(x^2+y^2)} - \frac{4(\alpha+e^{2im\phi})xZ_\pm j_n(\kappa_\pm)F_{nm}}{R_\pm^2(Z_\pm^2-R_\pm^2)} - \frac{2(\alpha+e^{2im\phi})x P_n^m(\cos\theta_\pm)\Psi_n}{R_\pm^2}$$
$$- \frac{i}{k}\Bigg[\frac{2(\alpha+e^{2im\phi})Z_\pm y\{j_n(\kappa_\pm)[2Z_\pm F_{nm}+\Lambda_{nm}]+Z_\pm F_{nm}\Psi_n\}}{R_\pm^4(R_\pm^2-Z_\pm^2)} - \frac{2i(e^{2im\phi}-\alpha)mx\big[P_n^m(\cos\theta_\pm)Z_\pm\Psi_n+2j_n(\kappa_\pm)F_{nm}\big]}{R_\pm^2(x^2+y^2)}$$
$$- \frac{2(\alpha+e^{2im\phi})yF_{nm}\Psi_n}{R_\pm^4} - \frac{(\alpha+e^{2im\phi})y P_n^m(\cos\theta_\pm)Z_\pm[\xi_n-2\Psi_n]}{R_\pm^4} - \frac{4(\alpha+e^{2im\phi})y(3Z_\pm^2-R_\pm^2)j_n(\kappa_\pm)F_{nm}}{R_\pm^4(R_\pm^2-Z_\pm^2)}\Bigg]\Bigg\}, \tag{A12}$$

$$H_{z,nm}^{(z,-z)} = E_{z,nm}^{(z,-z)}. \tag{A13}$$

[1] N. Lindlein and G. Leuchs, in *Handbook of Lasers and Optics*, edited by F. Träger (Springer, New York, 2007), Chap. 3.
[2] A. E. Siegman, *Lasers* (University Science Books, Mill Valley, CA, 1986).
[3] L. Mandel and E. Wolf, *Optical Coherence and Quantum Optics* (Cambridge University Press, Cambridge, UK, 1995).
[4] H. Kogelnik and T. Li, Appl. Opt. **5**, 1550 (1966).
[5] M. Lax, W. H. Louisell, and W. B. McKnight, Phys. Rev. A **11**, 1365 (1975).
[6] L. W. Davis, Phys. Rev. A **19**, 1177 (1979).
[7] J. P. Barton and D. R. Alexander, J. Appl. Phys. **66**, 2800 (1989).
[8] G. Gouesbet and G. Grehan, *Generalized Lorenz-Mie Theories*, 1st ed. (Springer, Berlin, 2011).
[9] J. A. Lock, J. Quant. Spectrosc. Radiat. Transfer **126**, 16 (2013).
[10] J. P. Barton, D. R. Alexander, and S. A. Schaub, J. Appl. Phys. **66**, 4594 (1989).
[11] G. P. Agrawal and D. N. Pattanayak, J. Opt. Soc. Am. **69**, 575 (1979).
[12] P. Varga and P. Török, Opt. Commun. **152**, 108 (1998).
[13] C. G. Chen, P. T. Konkola, J. Ferrera, R. K. Heilmann, and M. L. Schattenburg, J. Opt. Soc. Am. A **19**, 404 (2002).
[14] J. A. Lock, J. Opt. Soc. Am. A **23**, 2803 (2006).
[15] B. D. Seckler and J. B. Keller, J. Acoust. Soc. Am. **31**, 192 (1959).
[16] J. B. Keller and J. F. C. Karal, J. Appl. Phys. **31**, 1039 (1960).
[17] J. B. Keller and W. Streifer, J. Opt. Soc. Am. **61**, 40 (1971).
[18] G. A. Deschamps, Electron. Lett. **7**, 684 (1971).
[19] L. B. Felsen, J. Opt. Soc. Am. **66**, 751 (1976).
[20] A. L. Cullen and P. K. Yu, Proc. R. Soc. London, Ser. A **366**, 155 (1979).
[21] M. Couture and P.-A. Belanger, Phys. Rev. A **24**, 355 (1981).
[22] L. B. Felsen, Geophys. J. R. Astron. Soc. **79**, 77 (1984).
[23] B. T. Landesman and H. H. Barrett, J. Opt. Soc. Am. A **5**, 1610 (1988).
[24] C. J. R. Sheppard and S. Saghafi, Phys. Rev. A **57**, 2971 (1998).
[25] Z. Ulanowski and I. K. Ludlow, Opt. Lett. **25**, 1792 (2000).
[26] S. Orlov and U. Peschel, Phys. Rev. A **82**, 063820 (2010).
[27] F. G. Mitri, Phys. Rev. A **87**, 035804 (2013).
[28] F. G. Mitri, Phys. Rev. E **89**, 023205 (2014).
[29] S. Orlov and P. Banzer, Phys. Rev. A **90**, 023832 (2014).
[30] P. B. Bareil and Y. Sheng, J. Opt. Soc. Am. A **30**, 1 (2013).
[31] J. D. Jackson, in *Classical Electrodynamics*, 3rd ed. (Wiley, Hoboken, 1999), p. 240.
[32] J. Chen, J. Ng, K. Ding, K. H. Fung, Z. Lin, and C. T. Chan, Sci. Rep. **4**, 6386 (2014).
[33] F. G. Mitri, J. Quantum Spectrosc. Radiat. Transfer **182**, 172 (2016).
[34] F. G. Mitri, Phys. Rev. A **85**, 025801 (2012).
[35] F. G. Mitri, Eur. Phys. J. D **67**, 135 (2013).
[36] L. W. Davis and G. Patsakos, Opt. Lett. **6**, 22 (1981).
[37] F. N. H. Robinson, Phys. Rep. **16**, 313 (1975).
[38] I. Brevik, Phys. Rep. **52**, 133 (1979).
[39] S. M. Barnett, J. Opt. B: Quantum Semiclassical Opt. **4**, S7 (2002).
[40] F. G. Mitri, IEEE Trans. Ultrason., Ferroelectr. Freq. Control **61**, 191 (2014).
[41] A. V. Novitsky and D. V. Novitsky, J. Opt. Soc. Am. A **24**, 2844 (2007).
[42] M. A. Salem and H. Bağcı, Opt. Express **19**, 8526 (2011).
[43] P. Vaveliuk and O. Martinez-Matos, Opt. Express **20**, 26913 (2012).
[44] A. V. Novitsky and L. M. Barkovsky, Phys. Rev. A **79**, 033821 (2009).